

Large piezoelectric and elastic properties in B and Sc codoped wurtzite AlN

Cite as: J. Appl. Phys. **131**, 245108 (2022); <https://doi.org/10.1063/5.0090501>

Submitted: 07 March 2022 • Accepted: 05 June 2022 • Published Online: 29 June 2022

Huirong Jing, Yaowei Wang, Qiuhaio Wen, et al.



View Online



Export Citation



CrossMark

ARTICLES YOU MAY BE INTERESTED IN

Electron accumulation and distribution at interfaces of hexagonal $\text{Sc}_x\text{Al}_{1-x}\text{N}/\text{GaN}$ - and $\text{Sc}_x\text{Al}_{1-x}\text{N}/\text{InN}$ -heterostructures


Journal of Applied Physics **131**, 245702 (2022); <https://doi.org/10.1063/5.0094533>

Tutorial: Piezoelectric and magnetoelectric N/MEMS—Materials, devices, and applications


Journal of Applied Physics **131**, 241101 (2022); <https://doi.org/10.1063/5.0094364>

Crystal structure deformation and phase transition of AlScN thin films in whole Sc concentration range

Journal of Applied Physics **132**, 025103 (2022); <https://doi.org/10.1063/5.0087505>



HIDEN
ANALYTICAL



40 YEARS
1982-2022


Instruments for Advanced Science

- Knowledge,
- Experience,
- Expertise

Click to view our product catalogue


Contact Hiden Analytical for further details:
www.HidenAnalytical.com
info@hideninc.com

Gas Analysis




- ▶ dynamic measurement of reaction gas streams
- ▶ catalysis and thermal analysis
- ▶ molecular beam studies
- ▶ dissolved species probes
- ▶ fermentation, environmental and ecological studies

Surface Science




- ▶ UHVTPD
- ▶ SIMS
- ▶ end point detection in ion beam etch
- ▶ elemental imaging - surface mapping

Plasma Diagnostics



- ▶ plasma source characterization
- ▶ etch and deposition process reaction kinetic studies
- ▶ analysis of neutral and radical species

Vacuum Analysis



- ▶ partial pressure measurement and control of process gases
- ▶ reactive sputter process control
- ▶ vacuum diagnostics
- ▶ vacuum coating process monitoring

Large piezoelectric and elastic properties in B and Sc codoped wurtzite AlN

Cite as: J. Appl. Phys. 131, 245108 (2022); doi: 10.1063/5.0090501

Submitted: 7 March 2022 · Accepted: 5 June 2022 ·

Published Online: 29 June 2022



Huirong Jing,¹ Yaowei Wang,¹ Qiu hao Wen,¹ Xiaomeng Cai,¹ Ke Liu,¹ Weimin Li,² Lei Zhu,³ Xin Li,³ and Hong Zhu^{1,4,a}

AFFILIATIONS

¹Joint Institute, University of Michigan–Shanghai Jiao Tong University Joint Institute, Shanghai Jiao Tong University, Shanghai 200240, China

²Shanghai Institute of IC Materials, 333 Huangqing Road, Jiading District, Shanghai 201800, China

³Shanghai Institute of Microsystem and Information Technology, Chinese Academy of Sciences, Shanghai 200050, China

⁴Foshan (Southern China) Institute for New Materials, 92 Yanbu Suiyan West Road, Dali Town, Nanhai District, Foshan, Guangdong 528200, China

^aAuthor to whom correspondence should be addressed: hong.zhu@sjtu.edu.cn

ABSTRACT

Balancing the piezoelectric stress coefficient (e_{33}) and the elastic constant (C_{33}) of AlN-based materials is challenging but crucial for its application in bulk acoustic wave resonators. In this work, via first-principles calculations, we demonstrate that e_{33} and C_{33} can be simultaneously enhanced by adding boron (B) in the $\text{Sc}_x\text{Al}_{1-x}\text{N}$ system. Compared with $\text{Sc}_x\text{Al}_{1-x}\text{N}$, the large C_{33} in $\text{B}_{0.125}\text{Sc}_{x-0.125}\text{Al}_{1-x}\text{N}$ is caused by the shorter and stiffer B–N bonds, and the enhancement of e_{33} mainly comes from a larger sensitivity of atomic coordinates with respect to the strain ($|du/d\epsilon|$). Further investigation shows that the introduction of B in $\text{Sc}_x\text{Al}_{1-x}\text{N}$ significantly decreases the ratio of lattice parameter c over a due to the planar coordination preference of bulk BN, which is accompanied by an increased average $|du/d\epsilon|$ and e_{33} . Such a negative correlation can be attributed to the fact that $|du/d\epsilon|$ of N is proportional to the asymmetry of transversal bond strengths but inversely proportional to the overall average bond strengths around N atoms. Such a bonding character observed in this work could be beneficial to the design of wurtzite materials with large piezoelectric coefficients and high elastic constants.

Published under an exclusive license by AIP Publishing. <https://doi.org/10.1063/5.0090501>

I. INTRODUCTION

The increase in the high frequency band in 5G communication leads to the demand for superior filters.^{1,2} As the core component of the filter, the development of piezoelectric material with large piezoelectric coefficient and high sound speed is crucial for high-frequency resonance and filtering. Lead zirconate titanate (PZT) perovskite, as one of the well-known piezoelectric materials, exhibits excellent electromechanical coupling performance due to its high piezoelectric coefficient.^{3,4} However, toxicity (lead), low Curie temperature, and low mechanical stability make PZT less attractive. Therefore, it is necessary to find nontoxic materials with large piezoelectric response and good thermal stability in a wide temperature range. In this regard, wurtzite AlN becomes a potential candidate for resonator application due to high stiffness, high temperature stability, large sound speed, and good compatibility with complementary metal

oxide semiconductors (CMOS).^{5–9} However, the main disadvantage of AlN is the low piezoelectric coefficient, which limits its application in the broadband communication system. For resonator application, K^2Q is the figure of merit (K is the electromechanical coupling coefficient and Q is the mechanical quality factor) and proportional to the piezoelectric strain coefficient (e_{33}) and elastic constant (C_{33}).¹⁰ Therefore, the large e_{33} and C_{33} are necessary in microelectromechanical systems (MEMS), such as bulk acoustic wave (BAW) filters or surface acoustic wave (SAW) filters.

Recent experimental and computational works showed that the piezoelectric strain coefficient (d_{33}) of scandium (Sc) doped AlN has a significant increase (about 500%) at ~50% Sc content compared to pure AlN.^{11–14} It has been reported that Sc doping in AlN increases the sensitivity of atomic coordinates with respect to the external strain and, hence, the e_{33} . On the other hand, Sc

doping induces a competition between the wurtzite phase and the hexagonal phase of the alloy, which leads to elongated energy surface topology in the c/a direction and, hence, largely decreases the C_{33} .¹²

It appears to be difficult to optimize piezoelectric and elastic properties simultaneously with single element doping, and the enhancement of one performance is always accompanied by the degradation of another. However, it might be feasible to achieve simultaneous optimization or at least a balance of C_{33} and e_{33} with double elements doping.^{15–18} Tholander *et al.*¹⁹ studied the piezoelectric and elastic properties of AlN alloys with group-IIA/IIB and group-IVB elements, which have a larger C_{33} but a smaller e_{33} than $\text{Sc}_x\text{Al}_{1-x}\text{N}$. They concluded that the low e_{33} was attributed to the small energy difference between tetrahedral phases and layered hexagonal phases of $\text{II}_{0.5}\text{IV}_{0.5}\text{N}$, resulting in a weak competition between fourfold and fivefold local coordination geometries and, hence, a decreased sensitivity of atomic positions with respect to the strain, $du/d\epsilon$. Manna *et al.*²⁰ found that doping B or Y alone can increase C_{33} or e_{33} , respectively. Thus, they codoped B and Y in AlN and found that compared with ternary $\text{Y}_x\text{Al}_{1-x}\text{N}$, the C_{33} increased, while the e_{33} decreased only slightly. These results inspire us to investigate the possibility of quaternary AlN-based alloys with a large piezoelectric coefficient and an elastic constant as well as to understand the underlying mechanism and to obtain the design principles of advanced AlN-based piezoelectric materials.

In this work, the piezoelectric coefficient and the elastic constant of $\text{B}_{0.125}\text{Sc}_{x-0.125}\text{Al}_{1-x}\text{N}$ (BSAN) were investigated via density functional theory (DFT) calculations. Among AlN-based materials, $\text{Sc}_x\text{Al}_{1-x}\text{N}$ (SAN) has the largest piezoelectric response observed in the experiment so far. Therefore, the e_{33} and other relative properties of BSAN were compared with SAN in the present study. First, the formation energy and elastic tensor of SAN and BSAN were calculated to determine the phase and mechanical stability. Second, different contribution factors affecting piezoelectric response were discussed in details. Finally, the underlying mechanism behind the large piezoelectric response of BSAN was clarified in terms of bond strengths in SAN and BSAN and also verified in $\text{Sc}_x\text{Ga}_y\text{Al}_{1-x-y}\text{N}$ systems. These findings offer a new design method to optimize both the piezoelectric coefficient and the elastic constant, which might be beneficial for the fundamental research and practical applications of wurtzite structure-based resonators.

II. COMPUTATIONAL DETAILS

First-principles calculations based on the density functional theory (DFT) were performed within the Vienna *Ab initio* Simulation Package (VASP) using the projector augmented-wave (PAW) method.^{21,22} The wave functions were expanded in a plane-wave basis set with a kinetic energy cutoff of 520 eV. The exchange-correlation interaction was treated within the generalized gradient approximation (GGA) in the form of Perdew–Burke–Ernzerhof (PBE) format.²³ All computations and data analyses were performed using the Materials Project high-throughput softwares: pymatgen,²⁴ FireWorks,²⁵ and MPWorks (available at <http://www.github.com/materialsproject>).

For all calculations, the Γ -centered k -point meshes with a grid density of 5000 per atom were adopted. All structures are fully

relaxed until the total energy is less than 10^{-6} eV and the force on each atom is no more than 0.01 eV/Å. van der Waals interactions are not included in our calculation due to the slight impact (see Table S1 in the [supplementary material](#) for details). The piezoelectric tensors were calculated using the density functional perturbation theory (DFPT), and elastic tensors were computed using the stress–strain methodology^{26,27} by performing six independent components of the Green–Lagrange strain tensor with four magnitudes ($\pm 0.5\%$, $\pm 1\%$) for the original structure. Chemical bonding strength analyses were performed by the crystal orbital Hamilton population (COHP) method, which is implemented in the LOBSTER code.²⁸

The experimental work showed that the single-phase wurtzite BAlN film with 14.4% B content can be prepared successfully by MOCVD.²⁹ Therefore, considering the solubility of B in AlN, we adopted two alloyed AlN systems, namely, $\text{B}_{0.125}\text{Sc}_{x-0.125}\text{Al}_{1-x}\text{N}$ and $\text{Sc}_x\text{Al}_{1-x}\text{N}$ with x changing from 0.125 to 1 in an interval of 0.125 to better understand the doping effects of B and Sc. According to our calculation, the e_{33} and C_{33} fluctuate largely for different configurations at a particular doping concentration. Thus, we think the effect of atomic distributions on piezoelectric and stability properties is important but will be difficult to be comprehensively studied using a large supercell, especially considering the large number of configurations associated with the large supercell. To obtain a comprehensive understanding about configuration-dependent stability and piezoelectric properties, we use $2 \times 2 \times 1$ wurtzite and hexagonal supercells (16 atoms) for the following calculation, while for rocksalt structures, $2 \times 2 \times 2$ supercells (16 atoms) were applied. For each doping concentration of x , all possible configurations within the supercell used in this work are considered and the probabilities of each configuration (i) are further determined following the below equation:³⁰

$$p_i = n_i e^{-\beta \Delta H_i} / \sum_j n_j e^{-\beta \Delta H_j}, \quad (1)$$

where p_i is the probability of configuration i for a given concentration, β is the Boltzmann factor and equals to $1/k_B T$, ΔH_i is the formation energy, and n_i is the multiplicities of configuration i . We further calculate the ensemble averaged property \bar{O} over the configuration i with property O_i based on the equation $\bar{O} = \sum p_i O_i$. For ΔH_i , $P_{3,i}$, $C_{33,i}$, and $e_{33,i}$, O_i is the corresponding value at configuration i . P_3 is the spontaneous polarization and calculated by $P_3 = e/V \sum_k Z_{k,33}^* \Delta u_{k,3}$, where $Z_{k,33}^*$ is the c -direction components of the Born effective charge in the unit of e , $\Delta u_{k,3}$ is the displacement along the c -direction of the k th atom with respect to the ideal nonpolar hexagonal configuration, and V is the polar supercell's volume. For Born effective charge $Z_{33,i}$ and sensitivity of atomic positions with respect to strain $du/d\epsilon_i$, O_i is defined as $O_i = 1/n_k \sum_{n_k} O_{n_k}$, where n_k runs over all of the k -type atoms in a supercell (e.g., in $2 \times 2 \times 1$ supercells, n_{Sc} , n_{Al} , and n_{N} are 2, 6, and 8 for $\text{Sc}_{0.25}\text{Al}_{0.75}\text{N}$, respectively). Unless otherwise specified, the following properties are ensemble averaged value of all configurations at the corresponding concentration.

III. RESULTS

Formation energies of wurtzite (w -), hexagonal (h -), and rocksalt (rs -) $\text{Sc}_x\text{Al}_{1-x}\text{N}$ (SAN) and $\text{B}_{0.125}\text{Sc}_{x-0.125}\text{Al}_{1-x}\text{N}$ (BSAN) with respect

to wurtzite AlN, hexagonal BN, and rocksalt ScN according to

$$\Delta H(x) = E_{\text{B}_{0.125}\text{Sc}_{x-0.125}\text{Al}_{1-x}\text{N}} - 0.125E_{\text{BN}} - (x - 0.125)E_{\text{ScN}} - (1 - x)E_{\text{AlN}}, \quad (2)$$

where $E_{\text{B}_{0.125}\text{Sc}_{x-0.125}\text{Al}_{1-x}\text{N}}$, E_{BN} , E_{ScN} , and E_{AlN} are the total energies per formula of BSAN, BN, ScN, and AlN, respectively, and results are shown in Fig. 1. Figure 1(a) shows *w*-SAN is energetically favorable up to $x \sim 0.6$, above which the rocksalt phase is stable. Unlike SAN, the *w*-BSAN is the most stable phase in the whole doping concentration range, as shown in Fig. 1(b).

We found that the formation energies of SAN and BSAN systems in Fig. 1 are all positive, which is similar to the result of others.^{30,32} Thus, the formation of SAN and BSAN is not spontaneous through thermodynamic equilibrium synthesis routes.³³ However, the non-equilibrium process, such as radio frequency magnetron reactive co-sputtering, can overcome the solubility limits to synthesize supersaturated metastable alloys and has been successfully implemented for $\text{Sc}_x\text{Al}_{1-x}\text{N}$ alloys.^{34–37} From the structural point of view, the wurtzite structure with point group 6 mm exhibits spontaneous polarization and three nonvanishing independent piezoelectric components, while the rock salt structure with point group $m\bar{3}m$ has the centrosymmetric point and no polarization. Thus, only the structures with Sc doping concentration below 0.5 will be considered in the following calculations. Table S2 in the supplementary material provides the formation energy of SAN doped with other concentrations of boron (25%, 37.5%, and 50%), and the corresponding value is larger than that in the same doping concentration of the $\text{B}_{0.125}\text{Sc}_{x-0.125}\text{Al}_{1-x}\text{N}$ system and is likely to be difficult to be synthesized experimentally.

We further checked the mechanical stability of $\text{B}_{0.125}\text{Sc}_{x-0.125}\text{Al}_{1-x}\text{N}$ ($x \leq 0.5$) according to the Born criteria, and it requires that all eigenvalues of C_{ij} are positive.³⁸ Except $\text{B}_1\text{Sc}_2\text{Al}_5\text{N}_8$ -2, all models we considered are mechanically stable.

The piezoelectric coefficient along the *c* direction, e_{33} , can be written as

$$e_{33} = e_{33}^{\text{clamped}} + e_{33}^{\text{non-clamped}}, \quad (3)$$

in which the e_{33}^{clamped} term is electronic polarization caused by the strain along the *c* direction without relaxation of internal atoms in the supercell. The $e_{33}^{\text{non-clamped}}$ term describes the ionic polarization (*P*) due to the displacement of internal atoms (*u*) with respect to the macroscopic strain (ϵ) and can be determined by³⁹

$$e_{33}^{\text{non-clamped}} = \frac{dP}{du} \frac{du}{d\epsilon} = \frac{4eZ_{33}}{\sqrt{3}a^2} \frac{du}{d\epsilon}, \quad (4)$$

where *e* is the electronic charge, Z_{33} represents the *c*-direction component of the Born effective charge in the unit of *e*, *a* is the equilibrium lattice parameter, and $du/d\epsilon$ is the sensitivity of atomic coordinates with respect to the external strain in the *c*-axis.

Figures 2(a) and 2(b) show the variation of e_{33} and C_{33} of SAN and BSAN with different Sc concentrations; detailed results are listed in supplementary materials. With the increase in Sc, e_{33} shows a monotonic increasing trend, while C_{33} decreases monotonously, when $x = 0.5$, d_{33} ($\approx e_{33}/C_{33}$) of SAN increases nearly six times, this is consistent with the previous experimental and computational results of the SAN system.^{11,12,30} The detailed d_{33} for SAN and BSAN is shown in Table S1 in the supplementary material. Similar results of C_{33} of SAN are also reported in the previous work.^{19,30,31} In Fig. 2(a), the e_{33} of BSAN is larger than SAN for

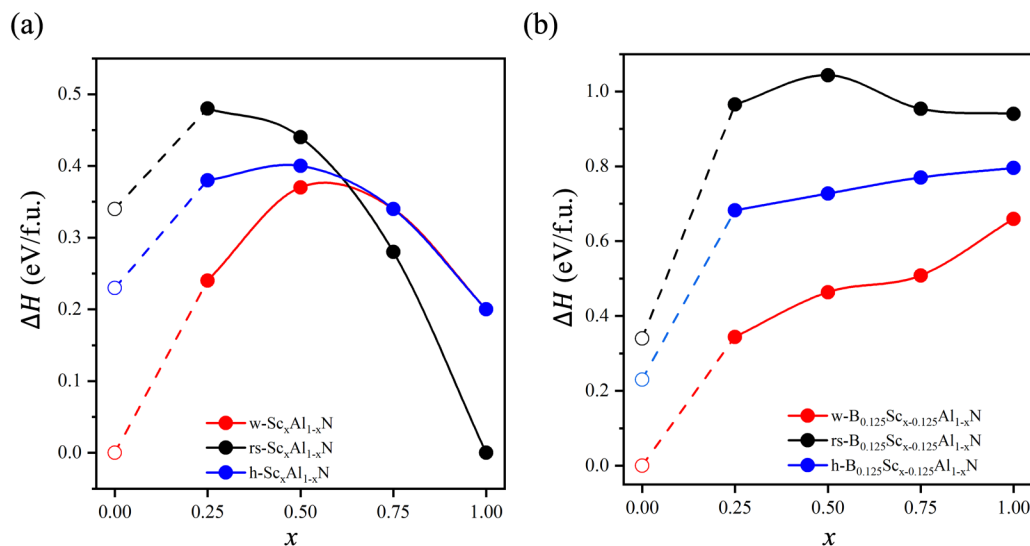


FIG. 1. Calculated formation energies (ΔH) of the wurtzite (*w*-), hexagonal (*h*-), and rocksalt (*rs*-) phases of (a) $\text{Sc}_x\text{Al}_{1-x}\text{N}$ and (b) $\text{B}_{0.125}\text{Sc}_{x-0.125}\text{Al}_{1-x}\text{N}$ as a function of doping concentration x .

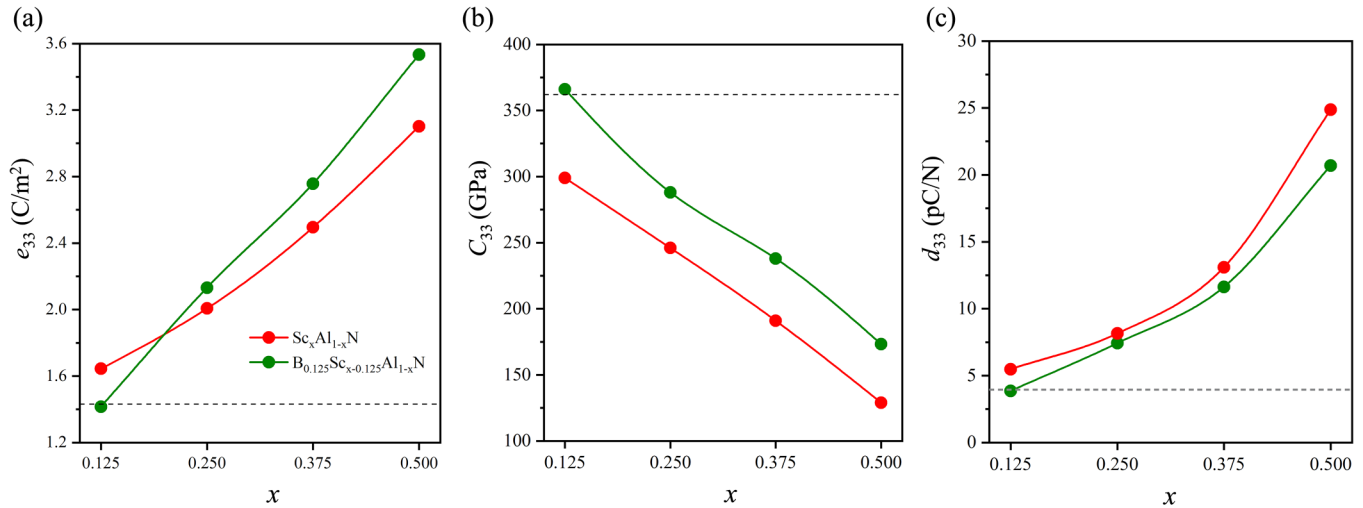


FIG. 2. The (a) piezoelectric stress coefficient e_{33} , (b) elastic constant C_{33} , and (c) piezoelectric strain coefficient d_{33} of wurtzite $\text{Sc}_x\text{Al}_{1-x}\text{N}$ and $\text{B}_{0.125}\text{Sc}_{x-0.125}\text{Al}_{1-x}\text{N}$. The dashed line corresponds to the values of pure AlN.

$x \geq 0.25$. When x equals to 0.5, the e_{33} values of BSAN and SAN are 2.42 times and 2.22 times larger than pure AlN, respectively. Figure 2(b) shows that C_{33} of BSAN is larger than that of SAN in all doping concentrations, and the difference in C_{33} between BSAN and SAN is almost a constant. In particular, the C_{33} of $\text{B}_{0.125}\text{Al}_{0.875}\text{N}$ is even larger than that of AlN, and this confirms the stronger bond strength of B–N than Al–N. Compared with SAN, the increase in C_{33} is greater than e_{33} of BSAN at the same doping concentration x , resulting in that d_{33} of SAN is slightly larger than that of BSAN, as shown in Fig. 2(c). Although we mainly focus on $\text{B}_{0.125}\text{Sc}_{x-0.125}\text{Al}_{1-x}\text{N}$, to give a comprehensive result, we also provide the piezoelectric coefficient of other doping concentrations of B and Sc in Table S1 in the [supplementary material](#).

It is worthwhile to compare the performance of BSAN with other AlN-based wurtzite materials. As shown in Table I, $\text{Yb}_{0.43}\text{Al}_{0.57}\text{N}$ and $\text{Mg}_{0.25}\text{Ti}_{0.25}\text{Al}_{0.5}\text{N}$ have a relatively large C_{33} but small e_{33} , and $\text{Mg}_{0.25}\text{Hf}_{0.25}\text{Al}_{0.5}\text{N}$ is the opposite. B and Sc codoped AlN is promising because it provides a large enhancement of e_{33} and relatively large C_{33} , though d_{33} may be slightly lower than pure Sc doping. The polarization P_3 (0.94 C/m^2) for $\text{B}_{0.125}\text{Sc}_{0.375}\text{Al}_{0.5}\text{N}$ is similar to pure Sc doping and slightly larger than that of well-known ferroelectric PbTiO_3 (0.81 C/m^2).⁴⁰ Hence, the possibility of polarization switching could make BSAN a promising candidate for ferroelectricity (detailed polarization results are displayed in Table S3 in the [supplementary material](#)). Ferroelectric properties will be further thoroughly studied in the future work. In this article, the origin of the e_{33} enhancement is comprehensively investigated.

As shown in Fig. 3(a) and 3(b), the increase in e_{33} in BSAN and SAN with Sc doping concentration is dominated by $e_{33}^{\text{non-clamped}}$, whose magnitude and variation are much larger than those of e_{33}^{clamped} . To better understand the variation of $e_{33}^{\text{non-clamped}}$, we plot the average and atom decomposed du/de and Z_{33} in Figs. 3(c)–3(f). The average $|du/de|$ appears to play a key role in

enhancing the piezoelectric coefficient upon Sc doping, while the variation of the Born effective charge is much smaller. For example, when x equals to 0.5, the average $|du/de|$ of BSAN is more than twice that of pure AlN, whereas $|Z_{33}|$ only increases by 12.7%. Moreover, we notice that although $|du/de|$ and $|Z_{33}|$ associated with B atoms are small, the addition of B doping will greatly enhance $|du/de|$ for Sc and Al cations, leading to larger average $|du/de|$ in BSAN compared to SAN for $x \geq 0.25$.

IV. DISCUSSION

The increased e_{33} of BSAN compared to SAN for $x \geq 0.25$ is found mainly comes from the larger atomic coordinate variation with respect to external strain upon the introduction of B, especially associated with Sc and Al cations. To better understand the underlying mechanism, we further investigated the crystal

TABLE I. Piezoelectric stress coefficient e_{33} (C/m²), piezoelectric strain coefficient d_{33} (pC/N), elastic constant C_{33} (GPa), and spontaneous polarization P_3 (C/m²) of BSAN and a few other AlN-based alloys.

Materials	e_{33}	d_{33}	C_{33} (GPa)	P_3	Reference
$\text{B}_{0.125}\text{Sc}_{0.375}\text{Al}_{0.5}\text{N}$	3.53	20.69	173	0.94	This work
$\text{Sc}_{0.5}\text{Al}_{0.5}\text{N}$	3.10	24.86	129	0.92	This work
$\text{Yb}_{0.43}\text{Al}_{0.57}\text{N}$	2.12	...	182	...	41
$\text{Cr}_{0.3}\text{Al}_{0.7}\text{N}$	2.59	19.52	42
$\text{Y}_{0.5}\text{Al}_{0.5}\text{N}$	3.0	18.75	160	...	20
$\text{Mg}_{0.25}\text{Ti}_{0.25}\text{Al}_{0.5}\text{N}$	2.2	12.5	175	...	19
$\text{Mg}_{0.25}\text{Zr}_{0.25}\text{Al}_{0.5}\text{N}$	2.7	19	142	...	19
$\text{Mg}_{0.25}\text{Hf}_{0.25}\text{Al}_{0.5}\text{N}$	3	23	130	...	19
$\text{Li}_{0.1875}\text{Ta}_{0.1875}\text{Al}_{0.625}\text{N}$	2.8	17.5	160	0.80	18
$\text{Li}_{0.1875}\text{Nb}_{0.1875}\text{Al}_{0.625}\text{N}$	2.6	15.7	165	0.84	18

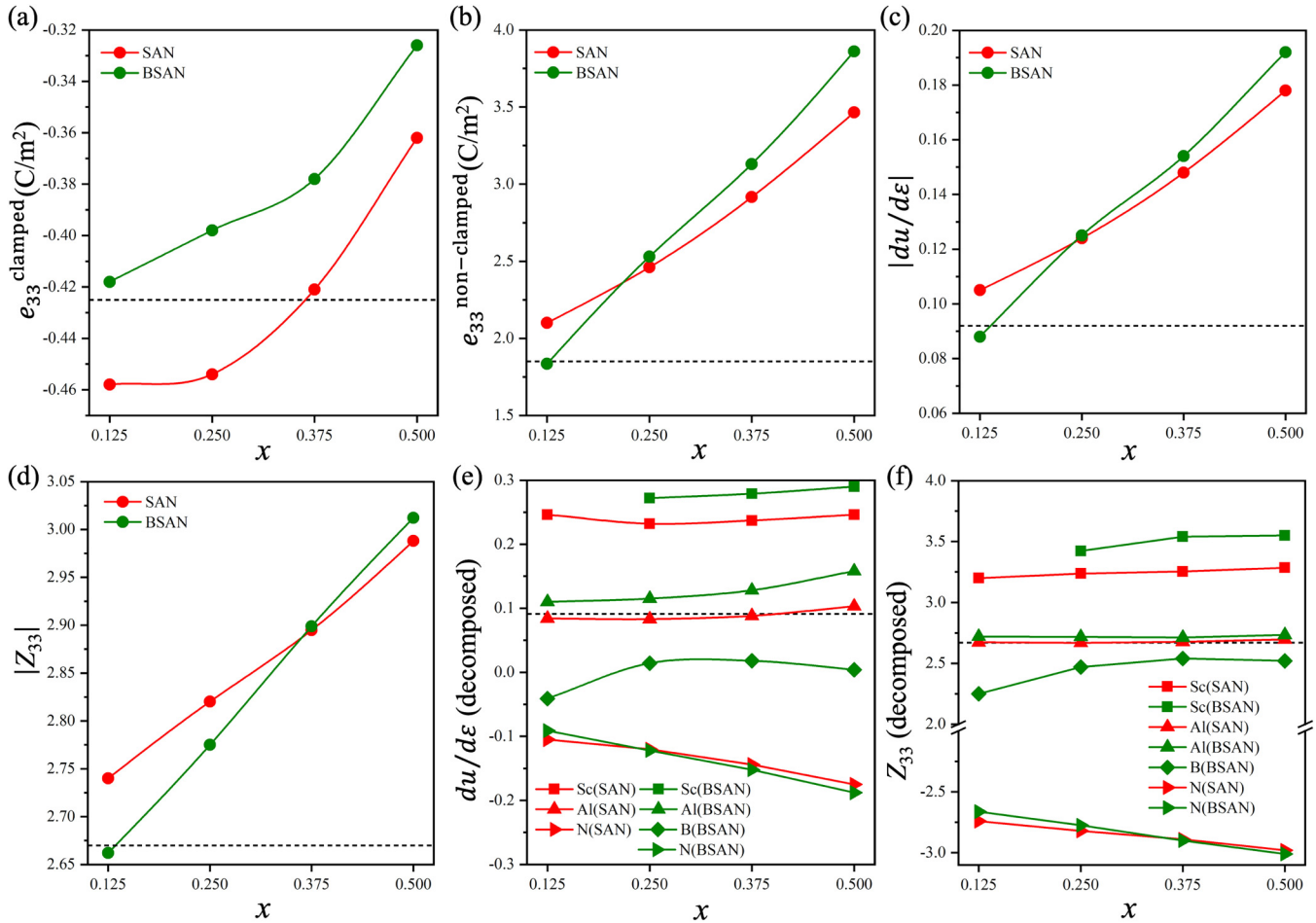


FIG. 3. Different contribution factors of the e_{33} of $\text{Sc}_x\text{Al}_{1-x}\text{N}$ and $\text{B}_{0.125}\text{Sc}_{0.375}\text{Al}_{0.5}\text{N}$. (a) shows the e_{33}^{clamped} term, (b) gives the $e_{33}^{\text{non-clamped}}$ term, (c) and (d) are the average $|du/d\epsilon|$ and $|Z_{33}|$ of cations (anions), and (e) and (f) are the atom decomposed $du/d\epsilon$ and Z_{33} . It should be noted that the average $du/d\epsilon$ (Z_{33}) of cations and anions has the same value but opposite sign.

structure and bonding characters in BSAN and SAN. Figures 4(a) and 4(b) display the structures of $\text{B}_{0.125}\text{Sc}_{0.375}\text{Al}_{0.5}\text{N}$ with the lowest energy before and after structural optimization. (Similar plots for other concentrations of BSAN and SAN are shown in Fig. S2 in the [supplementary material](#).) We note that after the structural optimization of BSAN, the N atoms around B atom changed from tetrahedral coordination (sp^3) to planar coordination (sp^2), while the latter is the most stable coordination mode for bulk BN. At the same time, the N atoms around Sc atom change from tetrahedral coordination to the fivefold coordination, whereas this change is not obvious in SAN. The direct influence of these structural changes is shown in Fig. 4(c). Compared with SAN, the breaking of B–N bond in BSAN leads to the lattice parameter a similar to that of SAN. The lattice parameter c of BSAN is much smaller than SAN, and the value of c remains almost unchanged with the increase in doping concentration. This can be attributed to two reasons: first and foremost, the

atomic radius of B is smaller than Sc and the bond length between B and N is shorter, which lead to the lattice parameter c of BSAN being shorter than that of SAN. Second, the introduction of B accelerates the lattice instability and the tetrahedral coordination of N around Sc degenerates into fivefold coordination, resulting in the lattice parameter c that remains to be almost a constant. A detailed analysis is shown in the [supplementary material](#) and Fig. S3 in the [supplementary material](#). To demonstrate the relationship between the structural change and the piezoelectric coefficient, the e_{33} of all configurations of BSAN and SAN as a function of c/a is plotted in Fig. 4(d). It can be seen that e_{33} has a negative linear correlation with the c/a ratio, which is consistent with the previous literature.⁴³ Since $|du/d\epsilon|$ plays a key role in enhancing the e_{33} [shown in Fig. 3(c)], the average and atom decomposed $|du/d\epsilon|$ of anion N at each c/a is plotted in Fig. S4 in the [supplementary material](#), and results are consistent with the trend in Fig. 4(d).

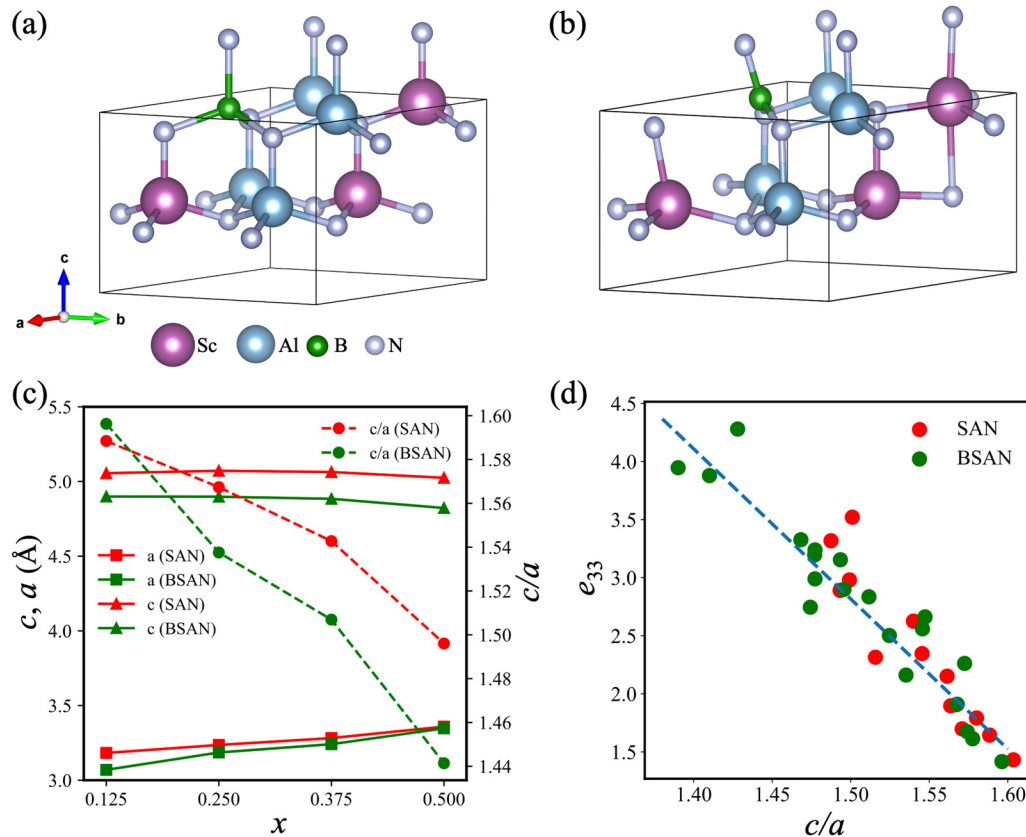


FIG. 4. Crystal structures of $B_{0.125}Sc_{0.375}Al_{0.5}N$ (a) before and (b) after structure optimization. (c) The lattice parameter (a , c , c/a) of SAN and BSAN at different doping concentrations. (d) The piezoelectric coefficient as a function of c/a ratio.

To better understand this collective behavior of various atoms in the quaternary system, we next try to identify how the atomic $|du/d\epsilon|$ is associated with local bonding characters. For simplicity, $|du/d\epsilon|$ and bond strengths (-ICOHP values⁴⁴) around N atoms are studied in details. It should be noted that the more positive the -ICOHP, the stronger the bond strength. To visualize these data, four bonds around N are classified into two types, i.e., three transversal bonds and one longitudinal bond, we define the average -ICOHP value of four bonds around N as B_{ave} , the average -ICOHP of three transverse bonds around N as B_{t-ave} , and the corresponding maximum absolute value of the difference of ICOHP of these three transversal bonds as B_{diff} , and all these values are positive and are used to represent bond strength. Figure S5 in the [supplementary material](#) displays all atomic environments around N in $B_{0.125}Sc_{0.375}Al_{0.5}N$, and the corresponding $|du/d\epsilon|$ of N and corresponding -ICOHP values around N are listed in Table S4 in the [supplementary material](#). We find that bond strengths increase from Sc-N and Al-N to B-N.

In Fig. 5, we use the obtained $|du/d\epsilon|$ of N and corresponding bond strength in the most stable structures for each concentration of SAN and BSAN to make a statistical analysis. As shown in

Fig. 5(a), a weak B_{t-ave} and B_{ave} will have a large $|du/d\epsilon|$, and heat map of different bond strengths and $|du/d\epsilon|$ with each other is shown in Fig. S6 in the [supplementary material](#). Then, three bond strength features, namely, B_{t-ave} , B_{ave} , and B_{diff} , are considered to perform linear regression. The regression results and expressions of $|du/d\epsilon|$ are displayed in Fig. 5(b). The schematic diagram in Fig. 5(b) shows that N atoms with a broken B-N bond have a larger $|du/d\epsilon|$, while the $|du/d\epsilon|$ is smaller for tetrahedral coordination. Thus, we conclude that a crystal with a weak overall average and average transversal bond strengths but a large absolute value of transversal bond strength difference can result in large $|du/d\epsilon|$.

An average value of $|du/d\epsilon|$ could better represent e_{33} according to the definition of the piezoelectric coefficient. In Fig. 5(c), we show average $|du/d\epsilon|$ of N in each configuration in Fig. 5(b), which is defined as $|du/d\epsilon|_{ave} = \frac{1}{n} \sum du_i/d\epsilon$, where i runs over all the N atoms in a supercell and n is the number of N in a supercell. Moreover, to verify the generality of the design criteria we obtained, we predicted the $|du/d\epsilon|$ and $|du/d\epsilon|_{ave}$ of 11 B and Sc co-doped AlN with larger supercells (namely, five configurations of $B_{0.0625}Sc_{0.625}Al_{0.875}N$ and five configurations of $B_{0.125}Sc_{0.125}Al_{0.75}N$ in $2 \times 2 \times 2$ supercells and one configuration of $B_{0.125}Sc_{0.125}Al_{0.75}N$

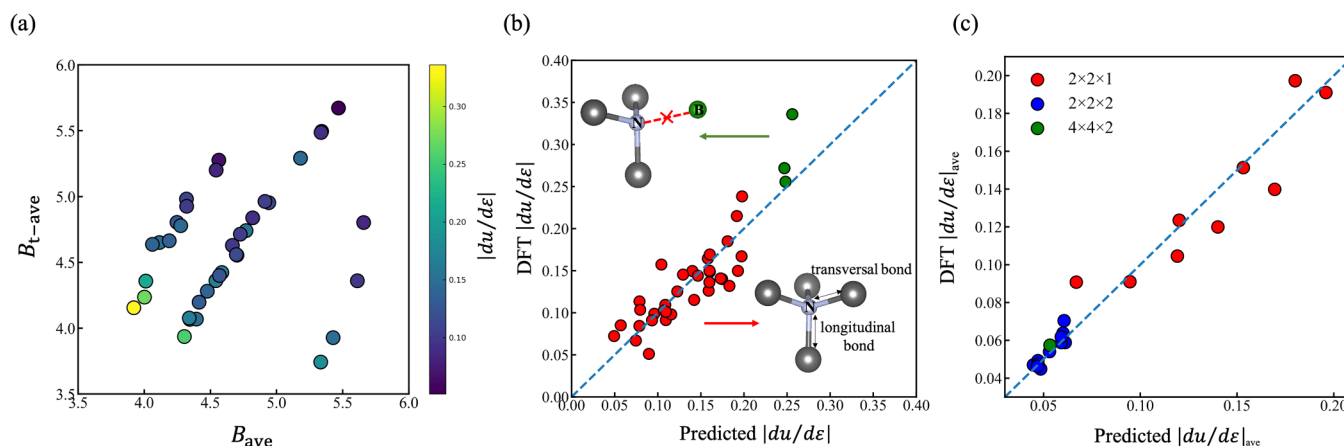


FIG. 5. (a) Correlations between the atom decomposed $|du/d\epsilon|$ of N and bond strength descriptors B_{ave} and B_{t-ave} in BSAN and SAN. The color of circle represents $|du/d\epsilon|$. (b) Correlations between the DFT calculated $|du/d\epsilon|$ and predicted $|du/d\epsilon|$. Insets show the coordination of N with the surrounding cations; green atom is B, light gray atoms are N, and dark gray atoms represent uncertain elements. The regression expression is $|du/d\epsilon| = -0.046B_{ave} - 0.074B_{t-ave} + 0.012B_{diff} + 0.674$. (c) Correlations between the DFT calculated average $|du/d\epsilon|$ and expression predicted average $|du/d\epsilon|$ of N in $2 \times 2 \times 1$, $2 \times 2 \times 2$, and $4 \times 4 \times 2$ supercells with different configurations.

in the $4 \times 4 \times 2$ supercell) based on the regression model obtained within $2 \times 2 \times 1$ supercells, and the result shows that the local bond strength-related expression is also applicable to the larger supercell. All configurations and $|du/d\epsilon|$ of each N atom in $4 \times 4 \times 2$ and $2 \times 2 \times 2$ supercells are displayed in Fig. 5(c) and Figs. S7 and S8 in the [supplementary material](#). As an extension, to give a more comprehensive study and testify our bond strength rules other than boron, we choose Sc and Ga co-doped AlN for further investigation, and results are demonstrated in Figs. S9 and S10 in the [supplementary material](#). Each subplot of Fig. S9 in the [supplementary material](#) shows that at a fixed concentration of Ga, e_{33} of $Sc_xGa_yAl_{1-x-y}N$ increased with the increase in Sc. However, all e_{33} values are smaller than that of SAN with the same doping concentration, while the formation energy is also lower. Figure S10 in the [supplementary material](#) shows the correlations between the DFT calculated $|du/d\epsilon|$ and predicted $|du/d\epsilon|$ of $Sc_xGa_yAl_{1-x-y}N$ and $B_{0.125}Sc_{x-0.125}Al_{1-x}N$ with the regression expression obtained from SAN and BSAN, and we found that $Sc_xGa_yAl_{1-x-y}N$ obeys the bond strength design rules. These extensions further prove that we can use bond strength as a useful descriptor for further high-throughput search of high piezoelectric coefficient materials in the future.

V. CONCLUSION

In this work, the phase and mechanical stability of wurtzite $B_{0.125}Sc_{x-0.125}Al_{1-x}N$ were determined by calculating the formation energy and the elastic tensor. Then, the piezoelectric and elastic properties of wurtzite $B_{0.125}Sc_{x-0.125}Al_{1-x}N$ alloys were studied in detail. Comparing to $Sc_xAl_{1-x}N$, $B_{0.125}Sc_{x-0.125}Al_{1-x}N$ shows a larger e_{33} when $x \geq 0.25$ and a larger C_{33} in the whole range of calculation. We found that the larger e_{33} of BSAN compared to SAN at the same concentration mainly comes from the larger atomic coordinate variation with respect to external strain upon the

introduction of B, especially associated with Sc and Al cations. Further crystal structure and bonding characters analysis indicate that the introduction of B in $Sc_xAl_{1-x}N$ significantly decreases the ratio of lattice parameter c to a , which is accompanied by an increased average $|du/d\epsilon|$ and e_{33} . This correlation can be attributed to the fact that a weak overall average and transversal average bond strength but a large absolute value of transversal bond strength difference can result in a large $|du/d\epsilon|$, hence a higher piezoelectric coefficient. Thus, the weak but asymmetric bonds in $B_{0.125}Sc_{x-0.125}Al_{1-x}N$ increase the e_{33} , while the formed B–N bonds also increase the C_{33} . Such a bonding mode in BSAN is the key to realize high piezoelectric response and low mechanical loss in wurtzite compounds.

SUPPLEMENTARY MATERIAL

See the [supplementary material](#) for details of the structure information; formation energy, bandgap, polarization, and piezoelectric coefficients, ICOHP values around N; the atom averaged and atom decomposed $|du/d\epsilon|$; correlations between the DFT calculated $|du/d\epsilon|$ and predicted $|du/d\epsilon|$ in Ga, Sc co-doped AlN; and heat map of features (bond strengths, $|du/d\epsilon|$) with each other. The elastic tensor of SAN and BSAN and structure files of $Sc_xGa_yAl_{1-x-y}N$ are freely available on GitHub (<https://github.com/jinghuiyong/BScAlN>).

ACKNOWLEDGMENTS

This work was supported by the Shanghai Technology Innovation Action Plan 2020-Integrated Circuit Technology Support Program (Project No. 20DZ1100603) and the Guangdong Province Key Area R&D Program (2019B010940001). All simulations were performed at the Shanghai Jiao Tong University High Performance Computing Center.

AUTHOR DECLARATIONS

Conflict of Interest

The authors have no conflicts to disclose.

Author Contributions

Huirong Jing: Data curation (lead); Formal analysis (equal); Investigation (lead); Methodology (lead); Validation (lead); Writing – original draft (lead). **Yaowei Wang:** Investigation (supporting); Methodology (supporting). **Qiu hao Wen:** Data curation (supporting); Investigation (supporting). **Xiaomeng Cai:** Investigation (supporting). **Ke Liu:** Software (supporting). **Weimin Li:** Conceptualization (supporting); Investigation (supporting). **Lei Zhu:** Conceptualization (supporting). **Xin Li:** Conceptualization (supporting). **Hong Zhu:** Formal analysis (equal); Writing – review & editing (equal).

DATA AVAILABILITY

The data that support the findings of this study are available within the article and its [supplementary material](#).

REFERENCES

- ¹K. M. Lakin, *IEEE Microw. Mag.* **4**, 61–67 (2003).
- ²S. Mahon, *IEEE Trans. Semicond. Manuf.* **30**, 494–499 (2017).
- ³R. Guo, L. E. Cross, S.-E. Park, B. Noheda, D. E. Cox, and G. Shirane, *Phys. Rev. Lett.* **84**, 5423 (2000).
- ⁴G. L. Smith, J. S. Pulskamp, L. M. Sanchez, D. M. Potrepka, R. M. Proie, T. G. Ivanov, R. Q. Rudy, W. D. Nothwang, S. S. Bedair, C. D. Meyer, and R. G. Polcawich, *J. Am. Ceram. Soc.* **95**, 1777–1792 (2012).
- ⁵N. Sinha, G. E. Wabiszewski, R. Mahameed, V. V. Felmetsger, S. M. Tanner, R. W. Carpick, and G. Piazza, *Appl. Phys. Lett.* **95**, 053106 (2009).
- ⁶M. A. Moram and S. Zhang, *J. Mater. Chem. A* **2**, 6042–6050 (2014).
- ⁷M. Benetti, D. Cannata, F. Di Pietrantonio, and E. Verona, *IEEE Trans. Ultrason. Ferroelectr. Freq. Control* **52**, 1806–1811 (2005).
- ⁸S. Figge, H. Kröncke, D. Hommel, and B. M. Epelbaum, *Appl. Phys. Lett.* **94**, 101915 (2009).
- ⁹T. Kim, J. Kim, R. Dalmau, R. Schlessner, E. Preble, and X. Jiang, *IEEE Trans. Ultrason. Ferroelectr. Freq. Control* **62**, 1880–1887 (2017).
- ¹⁰P. Muralt, J. Antifakos, M. Cantoni, R. Lanz, and F. Martin, *IEEE Int. Ultrason. Symp.* **1**, 315–320 (2005).
- ¹¹M. Akiyama, T. Kamohara, K. Kano, A. Teshigahara, Y. Takeuchi, and N. Kawahara, *Adv. Mater.* **21**, 593–596 (2009).
- ¹²F. Tasnádi, B. Alling, C. Höglund, G. Wingqvist, J. Birch, L. Hultman, and I. A. Abrikosov, *Phys. Rev. Lett.* **104**, 137601 (2010).
- ¹³K. R. Talley, S. L. Millican, J. Mangum, S. Siol, C. B. Musgrave, B. Gorman, A. M. Holder, A. Zakutayev, and G. L. Brennecke, *Phys. Rev. Mater.* **2**, 063802 (2018).
- ¹⁴M. A. Caro, S. Zhang, T. Riekkinen, M. Ylilampi, M. A. Moram, O. Lopez-Acevedo, J. Molarius, and T. Laurila, *J. Phys.: Condens. Matter* **27**, 245901 (2015).
- ¹⁵M. Uehara, H. Shigemoto, Y. Fujio, T. Nagase, Y. Aida, K. Umeda, and M. Akiyama, *Appl. Phys. Lett.* **111**, 112901 (2017).
- ¹⁶T. Yokoyama, Y. Iwazaki, Y. Onda, T. Nishihara, Y. Sasajima, and M. Ueda, *IEEE Trans. Ultrason. Ferroelectr. Freq. Control* **61**, 1322–1328 (2014).
- ¹⁷Y. Iwazaki, T. Yokoyama, T. Nishihara, and M. Ueda, *Appl. Phys. Express* **8**, 061501 (2015).
- ¹⁸M. Noor-A-Alam, O. Z. Olszewski, H. Campanella, and M. Nolan, *ACS Appl. Mater. Interface* **13**, 944–954 (2021).
- ¹⁹C. Tholander, F. Tasnádi, I. A. Abrikosov, L. Hultman, J. Birch, and B. Alling, *Phys. Rev. B* **92**, 174119 (2015).
- ²⁰S. Manna, G. L. Brennecke, V. Stevanović, and C. V. Ciobanu, *J. Appl. Phys.* **122**, 105101 (2017).
- ²¹G. Kresse and J. Furthmüller, *Comput. Mater. Sci.* **6**, 15–50 (1996).
- ²²G. Kresse and J. Furthmüller, *Phys. Rev. B* **54**, 11169 (1996).
- ²³J. P. Perdew, K. Burke, and M. Ernzerhof, *Phys. Rev. Lett.* **78**, 1396 (1997).
- ²⁴S. P. Ong, W. D. Richards, A. Jain, G. Hautier, M. Kocher, S. Cholia, D. Gunter, V. L. Chevrier, K. A. Persson, and G. Ceder, *Comput. Mater. Sci.* **68**, 314–319 (2013).
- ²⁵A. Jain, S. P. Ong, W. Chen, B. Medasani, X. Qu, M. Kocher, M. Brafman, G. Petretto, G.-M. Rignanese, G. Hautier, D. Gunter, and K. A. Persson, *Concurr. Comput. Pract. Exp.* **27**, 5037–5059 (2015).
- ²⁶M. De Jong, W. Chen, T. Angsten, A. Jain, R. Notestine, A. Gamst, M. Sluiter, C. Krishna Ande, S. van der Zwaag, J. J. Plata, C. Toher, S. Curtarolo, G. Ceder, K. A. Persson, and M. Asta, *Sci. Data* **2**, 150009 (2015).
- ²⁷X. Wu, D. Vanderbilt, and D. R. Hamann, *Phys. Rev. B* **72**, 035105 (2005).
- ²⁸S. Maintz, V. L. Deringer, A. L. Tchougréeff, and R. Dronskowski, *J. Comput. Chem.* **37**, 1030–1035 (2016).
- ²⁹X. Li, S. Wang, H. Liu, F. A. Ponce, T. Detchprohm, and R. D. Dupuis, *Phys. Status Solidi B* **254**, 1600699 (2017).
- ³⁰H. Momida, A. Teshigahara, and T. Oguchi, *AIP Adv.* **6**, 065006 (2016).
- ³¹C. Tholander, I. A. Abrikosov, L. Hultman, and F. Tasnádi, *Phys. Rev. B* **87**, 094107 (2013).
- ³²D. F. Urban, O. Ambacher, and C. Elsässer, *Phys. Rev. B* **103**, 115204 (2021).
- ³³L. Hultman, *Vacuum* **57**, 1–30 (2000).
- ³⁴C. Höglund, J. Birch, B. Alling, J. Bareño, Z. Czígány, P. Å. Persson, G. Wingqvist, A. Zukauskaitė, and L. Hultman, *J. Appl. Phys.* **107**, 123515 (2010).
- ³⁵A. M. Holder, S. Siol, P. F. Ndione, H. Peng, A. M. Deml, B. E. Matthews, L. T. Schelhas, M. F. Toney, R. G. Gordon, W. Tumas, J. D. Perkins, D. S. Ginley, B. P. Gorman, J. Tate, A. Zakutayev, and S. Lany, *Sci. Adv.* **3**, e1700270 (2017).
- ³⁶T. Yanagitani and M. Suzuki, *Appl. Phys. Lett.* **105**, 122907 (2014).
- ³⁷A. Žukauskaitė, C. Tholander, F. Tasnádi, B. Alling, J. Palisaitis, J. Lu, P. O. Å. Persson, L. Hultman, and J. Birch, *Acta Mater.* **94**, 101–110 (2015).
- ³⁸F. Mouhat and F. X. Coudert, *Phys. Rev. B* **90**, 224104 (2014).
- ³⁹F. Bernardini, V. Fiorentini, and D. Vanderbilt, *Phys. Rev. B* **56**, R10024 (1997).
- ⁴⁰B. A. Tuttle, D. A. Payne, and J. L. Mukherjee, *MRS Bull.* **19**, 20 (1994).
- ⁴¹J. Jia and T. Yanagitani, *Phys. Rev. Appl.* **16**, 044009 (2021).
- ⁴²S. Manna, K. R. Talley, P. Gorai, J. Mangum, A. Zakutayev, G. L. Brennecke, V. Stevanović, and C. V. Ciobanu, *Phys. Rev. Appl.* **9**, 034026 (2018).
- ⁴³H. Momida and T. Oguchi, *Appl. Phys. Express* **11**, 041201 (2018).
- ⁴⁴K. Hirata, H. Yamada, M. Uehara, S. A. Anggraini, and M. Akiyama, *J. Phys. Chem. Solids* **152**, 109913 (2021).